examination of the characteristics of BrdU positive-cells other than CD31, DCX, or NeuN. In addition, how these histological changes in fluvastatin-treated rats were mechanistically linked to improved outcome was not clarified. Further study is necessary to clarify these points.

Summary

Overall, delayed postischemic chronic fluvastatin treatment showed beneficial effects on the recovery of cognitive impairment after stroke by enhancement of neuritogenesis and of angiogenesis and a decrease in Aβ deposition and superoxide anion production. Further studies might show potential clinical utility to treat cognitive impairment in patients with ischemic stroke.

Acknowledgments

The authors thank Dr Masatsugu Horiuchi and Dr Masaru Iwai for their helpful advice on superoxide detection by dihydroethidium staining, and Dr Hiroshi Sato for assistance with MRI.

Sources of Funding

This work was partially supported by a Grant-in-Aid from the Organization for Pharmaceutical Safety and Research, a Grant-in-Aid from The Ministry of Public Health and Welfare, a Grant-in-Aid from Japan Promotion of Science, and a Grant-in-Aid from the Ministry of Education, Culture, Sports, Science, and Technology, of the Japanese Government.

Disclosures

Fluvastatin was donated from Novartis Pharma. Masataka Sata received Honoraria payment (modest) from Novartis Pharma. Ryuichi Morishita received honoraria payment (modest) and has an advisory board relationship to Novartis Pharma.

References

1. Sacks FM, Pfeffer MA, Moye LA, Rouleau JL, Rutherford JD, Cole TG, Brown L, Warnica JW, Arnold JM, Wun CC, Davis BR, Braunwald E. The effect of pravastatin on coronary events after myocardial infarction in patients with average cholesterol levels: cholesterol and recurrent events trial investigators. *N Engl J Med*. 1996;335:1001–1009.
2. Amarenco P, Tonkin AM. Statins for stroke prevention: disappointment and hope. *Circulation*. 2004;109:III44–49.
3. Moonis M, Kane K, Schwiderski U, Sandage BW, Fisher M. HMG-CoA reductase inhibitors improve acute ischemic stroke outcome. *Stroke*. 2005;36:1298–1300.
4. Chen J, Zhang C, Jiang H, Li Y, Zhang L, Robin A, Katakowski M, Lu M, Chopp M. Atorvastatin induction of VEGF and BDNF promotes brain plasticity after stroke in mice. *J Cereb Blood Flow Metab*. 2005;25:281–290.
5. Chen J, Zhang ZG, Li Y, Wang Y, Wang L, Jiang H, Zhang C, Lu M, Katakowski M, Feldkamp CS, Chopp M. Statins induce angiogenesis, neurogenesis, and synaptogenesis after stroke. *Ann Neurol*. 2003;53:743–751.
6. Zhang L, Zhang ZG, Ding GL, Jiang Q, Liu X, Meng H, Hozeska A, Zhang C, Li L, Morris D, Zhang RL, Lu M, Chopp M. Multitargeted effects of statin-enhanced thrombolytic therapy for stroke with recombinant human tissue-type plasminogen activator in the rat. *Circulation*. 2005;112:3486–3494.
7. Belayev L, Alonso OF, Busto R, Zhao W, Ginsberg MD. Middle cerebral artery occlusion in the rat by intraluminal suture: neurological and pathological evaluation of an improved model. *Stroke*. 1996;27:1616–1623.
8. Sata M, Nishimatsu H, Osuga J, Tanaka K, Ishizaka N, Ishibashi S, Hirata Y, Nagai R. Statins augment collateral growth in response to ischemia but they do not promote cancer and atherosclerosis. *Hypertension*. 2004;43:1214–1220.
9. Nakatomi H, Kuriu T, Okabe S, Yamamoto S, Hatano O, Kawahara N, Tamura A, Kirino T, Nakafuku M. Regeneration of hippocampal pyramidal neurons after ischemic brain injury by recruitment of endogenous neural progenitors. *Cell*. 2002;110:429–441.
10. Petullo D, Masonic K, Lincoln C, Wibberley L, Teliska M, Yao DL. Model development and behavioral assessment of focal cerebral ischemia in rats. *Life Sci*. 1999;64:1099–1108.
11. Cavaglia M, Dombrowski SM, Drazba J, Vasanji A, Bokesch PM, Janigro D. Regional variation in brain capillary density and vascular response to ischemia. *Brain Res*. 2001;910:81–93.
12. van Groen T, Puurunen K, Maki HM, Sivenius J, Jolkkonen J. Transformation of diffuse beta-amyloid precursor protein and beta-amyloid deposits to plaques in the thalamus after transient occlusion of the middle cerebral artery in rats. *Stroke*. 2005;36:1551–1556.
13. Iwai M, Liu HW, Chen R, Ide A, Okamoto S, Hata R, Sakanaka M, Shiuchi T, Horiuchi M. Possible inhibition of focal cerebral ischemia by angiotensin II type 2 receptor stimulation. *Circulation*. 2004;110:843–848.
14. Robinson RG. Differential behavioral and biochemical effects of right and left hemispheric cerebral infarction in the rat. *Science*. 1979;205:707–710.
15. DeVries AC, Nelson RJ, Traystman RJ, Hurn PD. Cognitive and behavioral assessment in experimental stroke research: Will it prove useful? *Neurosci Biobehav Rev*. 2001;25:325–342.
16. Badan I, Platt D, Kessler C, Popa-Wagner A. Temporal dynamics of degenerative and regenerative events associated with cerebral ischemia in aged rats. *Gerontology*. 2003;49:356–365.
17. Badan I, Dinca I, Buchhold B, Suofu Y, Walker L, Gratz M, Platt D, Kessler CH, Popa-Wagner A. Accelerated accumulation of n- and c-terminal beta app fragments and delayed recovery of microtubule-associated protein 1b expression following stroke in aged rats. *Eur J Neurosci*. 2004;19:2270–2280.
18. Schabitz WR, Berger C, Kollmar R, Seitz M, Tanay E, Kiessling M, Schwab S, Sommer C. Effect of brain-derived neurotrophic factor treatment and forced arm use on functional motor recovery after small cortical ischemia. *Stroke*. 2004;35:992–997.
19. Endres M, Laufs U, Liao JK, Moskowitz MA. Targeting enos for stroke protection. *Trends Neurosci*. 2004;27:283–289.
20. Gonzalez-Billault C, Avila J, Caceres A. Evidence for the role of map1b in axon formation. *Mol Biol Cell*. 2001;12:2087–2098.
21. Pooler AM, Xi SC, Wurtman RJ. The 3-hydroxy-3-methylglutaryl co-enzyme a reductase inhibitor pravastatin enhances neurite outgrowth in hippocampal neurons. *J Neurochem*. 2006;97:716–723.
22. Wei L, Erinjeri JP, Rovainen CM, Woolsey TA. Collateral growth and angiogenesis around cortical stroke. *Stroke*. 2001;32:2179–2184.
23. Alexandrov AV, Hall CE, Labiche LA, Wojner AW, Grotta JC. Ischemic stunning of the brain: Early recanalization without immediate clinical improvement in acute ischemic stroke. *Stroke*. 2004;35:449–452.
24. Fassbender K, Simons M, Bergmann C, Stroick M, Lutjohann D, Keller P, Runz H, Kuhl S, Bertsch T, von Bergmann K, Hennerici M, Beyreuther K, Hartmann T. Simvastatin strongly reduces levels of Alzheimer's disease beta -amyloid peptides Abeta 42 and Abeta 40 in vitro and in vivo. *Proc Natl Acad Sci U S A*. 2001;98:5856–5861.
25. Casu MA, Wong TP, De Koninck Y, Ribeiro-da-Silva A, Cuello AC. Aging causes a preferential loss of cholinergic innervation of characterized neocortical pyramidal neurons. *Cereb Cortex*. 2002;12:329–337.
26. Jeljeli M, Strazielle C, Caston J, Lalonde R. Effects of ventrolateral-ventromedial thalamic lesions on motor coordination and spatial orientation in rats. *Neurosci Res*. 2003;47:309–316.
27. Rudin M, Baumann D, Ekatodramis D, Stirnimann R, McAllister KH, Sauter A. MRI analysis of the changes in apparent water diffusion coefficient, t(2) relaxation time, and cerebral blood flow and volume in the temporal evolution of cerebral infarction following permanent middle cerebral artery occlusion in rats. *Exp Neurol*. 2001;169:56–63.
28. Kawashima S, Yamashita T, Miwa Y, Ozaki M, Namiki M, Hirase T, Inoue N, Hirata K, Yokoyama M. HMG-CoA reductase inhibitor has protective effects against stroke events in stroke-prone spontaneously hypertensive rats. *Stroke*. 2003;34:157–163.
29. Sumi D, Hayashi T, Thakur NK, Jayachandran M, Asai Y, Kano H, Matsui H, Iguchi A. A HMG-CoA reductase inhibitor possesses a potent anti-atherosclerotic effect other than serum lipid lowering effects–the relevance of endothelial nitric oxide synthase and superoxide anion scavenging action. *Atherosclerosis*. 2001;155:347–357.
30. Morita H, Saito Y, Ohashi N, Yoshikawa M, Katoh M, Ashida T, Kurihara H, Nakamura T, Kurabayashi M, Nagai R. Fluvastatin ameliorates the hyperhomocysteinemia-induced endothelial dysfunction: The antioxidative properties of fluvastatin. *Circ J*. 2005;69:475–480.
31. Endres M. Statins and stroke. *J Cereb Blood Flow Metab*. 2005;25:1093–1110.

特集論文／分子イメージング時代の画像解析・データ解析の新しい視点

マイクロ SPECT を用いた小動物イメージングの定量的機能評価

Quantitative Functional Imaging of Small Animals Using MicroSPECT

銭谷　勉*
Tsutomu ZENIYA

要　旨

創薬や新規治療法の評価を目的とした前臨床研究において，小動物モデルを用いた in vivo イメージングは不可欠である．その中でも PET や SPECT などの高感度トレーサ技術である核医学的手法は生体内の生理機能を定量評価できるため大きな役割を果たしている．本論文では，小動物イメージングにおける定量的機能評価の意義および応用領域について言及した上で，マイクロ SPECT における動態解析および画像再構成の定量性について概論する．また，マイクロ SPECT を利用した定量的機能評価の例を紹介する．

キーワード：小動物，定量的機能評価，SPECT，ピンホールコリメータ，画像再構成

In vivo imaging of small laboratory animals facilitates objective assessment of pharmaceutical development and regenerative therapy in pre-clinical studies. Radionuclide imaging such as PET or SPECT is especially important because it allows to quantitatively assess physiological functions due to high sensitive tracing technique. This paper describes the significances and applications of quantitative functional assessment in small animal imaging, and then discusses quantitation about kinetic analysis and image reconstruction in microSPECT. Finally, it introduces quantitative functional imaging studies using microSPECT.

Key words: Small animal, Quantitative functional imaging, SPECT, Pinhole collimator, Image reconstruction
Med Imag Tech **26**(1): 14-20, 2008

1. はじめに

創薬や新規治療法を目的とした前臨床研究において，ラットやマウスなどの小動物モデルを用いた in vivo イメージングは不可欠である．また，近年の分子イメージング分野の発展に伴い，小動物専用の X 線 CT（Computed Tomography），MRI（Magnetic Resonance Imaging），PET（Positron Emission Tomography），SPECT（Single Photon Emission CT）および光イメージングなどの装置が盛んに開発されている．その中でも，PET や SPECT などの放射性同位元素をトレーサとして用いる核医学検査手法は，高い感度を有し，トレーサの集積の対して正確に比例した信号強度を提示するため，病態生理や病態生化学的な変化を定量に評価することが可能であるため重要な役割を果たしている．

PET 装置は高い感度を有するが，高解像度の小動物用 PET 装置でもその空間解像度は 1 mm を超えておらず〔1〕，小病変の画像化に不十分である．PET は放射線同位元素から放出される陽電子が電子と結合する際に反対方向に放出される 2 本の消滅放射線をリング状の検出器で同時計測することで，放射線同位元素の存在する位置を推定する．陽電子が静止するまでの距離を陽電子の飛程と呼ぶが，核種によっては飛程が装置の空間解像度よりも大きく，解像度を悪化させる．たとえば，^{15}O の場合，陽電子のエネルギーが高く，陽電子が消滅するまでに水中で平均 2.5 mm 移動する．また，PET 核種は半減期が短いため，小動物実験において，同一の個体の

* 国立循環器病センター研究所先進医工学センター放射線医学部〔〒 565-8565 大阪府吹田市藤白台 5-7-1〕：National Cardiovascular Center Research Institute.
e-mail: zeniya@ri.ncvc.go.jp
論文受付：2007 年 12 月 25 日
最終稿受付：2008 年 1 月 7 日

繰り返し撮像が行いやすいという利点である反面，サイクロトロンや放射性薬剤合成装置などの大掛かりな設備を必要とする．一方，SPECT装置は放射線同位元素から放出されるガンマ線の飛来方向を特定するためのコリメータを必要とするため，コリメータを必要としないPETに比べ感度が劣るのは避けられないが，コリメータの工夫次第ではPETよりも高い空間解像度が得られる．ピンホールコリメータは対象物がコリメータに近いほど感度および空間解像度を高くできるので（**Fig. 1**），小動物イメージングに適しており，1 mm以下の解像度が比較的容易に実現できる〔2,3〕．ほとんどの小動物用SPECT装置（マイクロSPECT）ではこのピンホールコリメータを利用している．感度が低いという問題は，複数のピンホールを利用することで克服する試みが行われている〔4～6〕．また，**Table 1**に示されているようにSPECT検査で使用される放射性核種は半減期が長いため，PETでは観測できない，長時間における薬剤の動態を観察したいという場合に適している．そして，何よりも放射性薬剤を他施設から入手できるため，安価で手軽に検査が実施できるという大きな利点がある．

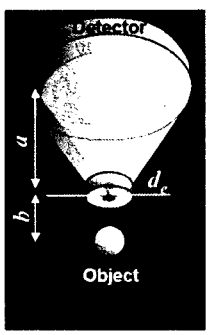

Geometric resolution (R_g)

$$R_g = (a+b)\frac{d_e}{a}$$

d_e: effective pinhole diameter

System resolution (R_o)

$$R_o = \sqrt{R_g^2 + \frac{b}{a}R_i^2}$$

R_i: intrinsic detector resolution

Resolution $\propto d_e \times (a+b)/a$
Sensitivity $\propto d_e^2/b^2$

Fig. 1 Physics of pinhole SPECT. Spatial resolution and sensitivity can be improved by positioning a collimator closer to an object.

従来のピンホールSPECTは，体軸方向に画像が歪み，視野内の解像度が不均一になるという問題があったため，定量評価が困難であった．著者らは，この原因をデータの不完全性によるものと仮説をたて，撮像軌道をラドン変換の完全性を満たすように設計し，立体的な画像再構成理論を導入することで，歪みのない視野全体で均一な解像度を有する3次元画像を得ることに成功した〔7〕．その結果，ピンホールSPECTにおいても小動物PET同様に定量評価が可能になった．しかしながら，PETやSPECTが得意とする，定量的な機能評価をマイクロSPECTで行う試みは，それほど広くなされていない．

本論文では，小動物イメージングにおける定量的機能評価に必要とされる著者らの物理工学的な最近の進歩について述べる．最初に，小動物イメージングの定量的機能評価の意義および応用領域について言及した上で，マイクロSPECTにおける動態解析および画像再構成の定量性ついて概論する．最後に，著者らが開発したマイクロSPECT装置を利用した定量的機能評価の例を紹介する．

2. 小動物イメージングにおける定量的機能評価の意義と応用領域

通常，遺伝子改変や病態モデル動物はマウスやラットなどの小動物に対して行われており，生きたまま，小動物内の分子をイメージングする技術は非常に重要である．とくに，ヒトから実

Table 1 Representative radionuclides used in SPECT study.

Isotope	Energy	Half life	Tracer	Application
^{99m}Tc	140 keV	6.01 hr	MDP/HMDP	bone scan
			MIBI	myocardial perfusion
			tetrofosmin	myocardial perfusion
			TRODAT	dopamine transporter
^{201}Tl	70 keV	72.9 hr	TlCl	myocardial perfusion
^{123}I	159 keV	13.3 hr	BMIPP	beta-oxidation
			MIBG	sympathetic
			β-CIT	dopamine transporter
			Iomazenil	benzodiazepine receptor
^{131}I	364 keV	8.04 day		thyroid
^{67}Ga	93, 185, 300 keV	3.26 day	citrate	tumor

験小動物まで同じ手技で定量的機能評価が可能な核医学イメージング技術は，血流などの生理的機能から種々の受容体，遺伝子発現，ペプチド・タンパクなどの疾患関連物質の体内動態までを観察できるため，創薬の迅速化・低コスト化や，テーラーメード医療，遺伝子治療，再生医療などに代表される新しい病気の診断・治療法の開発に大きく貢献するといわれている．

創薬においては，治療化合物の探索から体内吸収・体内動態の評価，臨床試験早期に必要な毒性と薬効評価，投与量の最適化などの分野においての利用が開始されている．再生医療分野においても，多くの局面で本質的な情報を提示し，有効な治療法の確立に向けて重要な役割を果たすことは明らかである．たとえば，心筋梗塞部位での血管新生治療，細胞移植治療では，細胞の定着や血管の発達などの形態的な再生だけでなく，生体の一部の組織として機能評価を行うことが必要である．定着した細胞および組織の血流がどの程度回復し，種々の生理的な負荷などによって本来持つべき反応力（血流の自動調節能と血管反応性，代謝の制御，神経連絡過程など）をどの程度有し，必要な生体フィードバックを可視化できることが望ましい．これらの分野の基盤技術を整備するためには，疾患の本質を理解すること，そのための基礎，前臨床，および臨床研究を並行して実施すること，また，本質的な治療実施のための各種基盤技術を有していることが不可欠である．

3. マイクロ SPECT による定量的機能評価の問題点

SPECT データから，血流量，結合能などの定量的な生理パラメータを得るためには，コンパートメントモデル解析やグラフ解析など，トレーサの動態解析を行う必要がある〔8〕．このとき，入力関数と呼ばれる動脈中の放射能濃度の投与時からの時間変化が必要となる．ヒトの場合，通常，腕の動脈に穿刺し，撮像中にマニュアルで頻回採血やポンプを用いた連続採血を行って入力関数を得る〔9〕．ラットやマウスの血液量は，ヒトに比べて少量のため，採血量が多くなると貧血を起こし，生理状態も大きく変化する．そのため，最低限の採血量に抑える必要があり，動脈と静脈を短絡させる arteriovenous（AV）シャント術を施し，そこから入力関数を得る方法が提案されている．

心筋機能の定量では，撮像された左心室から入力関数を得る方法が用いられる．しかし，これらの方法で得られる入力関数はあくまでも全血の放射能濃度であり，放射性薬剤が体内で代謝される場合，代謝産物の定量も行う必要もある．微量の血液中の代謝産物の定量は非常に困難である．このため，あらかじめ複数の同一動物で測定した平均入力関数を用いる方法や，入力関数の代わりにリファレンス領域を用いる方法〔10〕がしばしば使われる．

得られたパラメータを解釈する際には，ヒトとの違いを考慮する必要がある．代謝速度はヒトと小動物では大きく異なる．通常，小動物の撮像は麻酔下で行われるが，麻酔の影響も無視できない．著者らは覚醒下に適したラット専用のホルダーを作製し，1 週間の馴化を行うことによって，覚醒下でのラット心筋血流定量測定および血管反応性の評価を可能にした．

4. マイクロ SPECT 画像再構成における定量性

前述のようなトレーサの動態解析を行う場合，SPECT 画像の定量性が確保されていることが前提である．マイクロ SPECT 画像再構成においても，定量性を劣化させる要因を十分に考慮する必要がある．

1）部分容積効果

核医学装置は，定量性が高いとしばしばいわれるが，部分容積効果（小さい対象物を空間解像度の悪い装置で撮像したとき発生する測定値の過小評価）は大きく定量性に影響する．とくに，小動物の場合サイズがヒトより小さいため，相応の高い空間解像度が要求される．たとえば，臨床で利用されている PET 装置は 5 mm 程度の空間解像度を持つが，この装置で得られた画像と同等の解像度でラットを撮像したければ 0.6 mm，マウスでは 0.4 mm の空間解像度が要求される〔1〕．実際の小動物用 PET の空間解像度は 1～2 mm 程度であるため，部分容積効果は小動物 PET ではヒトよりも大きな問題となる．これに対して，小動物用のピンホール SPECT では数百 μm の空間解像度を実現できるため，部分容積効果を抑制できる点で優位である．しかしなが

ら，部分容積効果の定量性に与える影響は少なくないため，定量する際は十分に考慮する必要がある．コリメータ開口補正技術〔11〕などを用いて解像度を改善するのも1つの方策である．

2）吸収・散乱

SPECT で定量性を劣化させる大きな要因として，被写体内でのガンマ線の吸収および散乱がある．一般的な臨床脳 SPECT 検査では，60 ～ 80% の光子が体内での吸収を受け，30 ～ 40% の光子が散乱によって偽りの信号を与える．これらの影響を補正しなければ定量評価は難しい．飯田らは，実用的な手法によって吸収・散乱の影響を高い精度で補正することに成功し，SPECT でも PET 同様の定量評価を可能にした〔12〕．しかしながら，体内での吸収・散乱の影響は被写体の大きさに依存することを考えると，小動物ではヒトの場合に比べてそれほど大きくないと考えられる．Wang らはマウスにおける吸収・散乱の影響を，シミュレーションおよびファントム実験にて評価した．吸収も散乱も補正しない場合，15% 過小評価し，吸収補正のみ行った場合，9% 過大評価する．吸収と散乱の両方を補正して誤差は3%以下にできると報告している〔13〕．Deloar らは散乱線の影響に加え，ピンホールコリメータを突き抜けるガンマ線の影響も考慮する必要があることをシミュレーションによって示している〔14〕．この突き抜けガンマ線の影響はピンホール形状を knife-edge 型に代えて，keel-edge（channel-edge とも呼ぶ）型を使用することで抑制することができる〔15〕．

3）データの完全性

ピンホールコリメータを用いた SPECT 装置は原理上，3 次元収集を行っているが，コーンビーム型の 3 次元画像再構成法が必要となる．ピンポール SPECT において単一の円軌道でデータを収集した場合，体軸方向に画像が歪み，空間解像度が不均一となるため，定量解析は困難である．画像再構成法を解析的手法の FBP（Filtered Back-Projection）に代えて，OSEM（Ordered Subsets Expectation Maximization）などの統計学に基づいた逐次近似画像再構成法を使用することによって改善されるが，視野周辺では依然として解像度の劣化は残っている〔16〕．最近の研究で，著者らはこの原因をデータの不完全性に起因するものと仮説をたて，撮像軌道をラドン変換の完全性を満たすような複数回転軸軌道とし，これに立体的画像再構成理論を導入することで，視野内で均一な高解像度を得ることに成功した（**Fig. 2**）〔7〕．Metzler らはヘリカル軌道で完全データ収集を実現している〔17〕．従来は定性的な評価のみに利用されてきた高解像度撮像法のピンホール SPECT だが，この問題の解決によって PET 同様に定量解析が可能になった．

4）トランケーション

ピンホールコリメータは対象物がコリメータに近いほど感度および解像度を高くできるのが特長であるが，極端に近づけるとトランケーション（データの欠損）が生じ，再構成画像のカウントは過大評価され，定量評価の妨げとなる．通常は被写体が視野から外れないように，被写

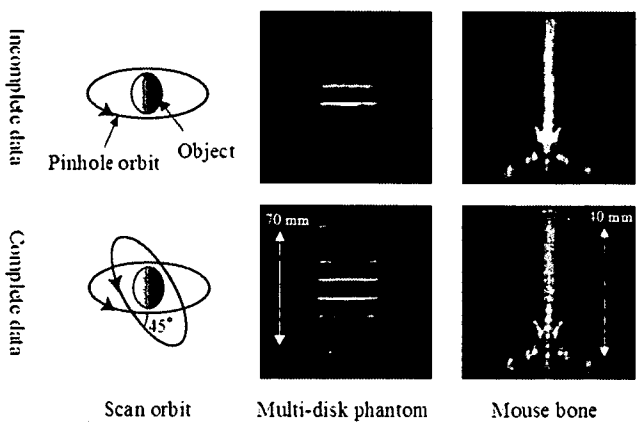

Fig. 2 Comparison between conventional acquisition and complete data acquisition in multi-disk phantom study and mouse bone scan with ^{99m}Tc. Data acquired by conventional single circular orbit are incomplete. Complete data are acquired by two-circular orbit. Complete data improve axial blurring and non-uniform spatial resolution in pinhole SPECT.

体からコリメータをある程度離して撮像する．ただし，これは解像度と感度を妥協することになる．著者らは，Defrise らが 2 次元 X 線 CT を対象として提案した理論〔18〕を基に，ピンホール SPECT でトランケーションを許す 3 次元画像再構成法 TC-OSEM（Truncation Compensated OSEM）を開発した〔19〕．本画像再構成理論では，**Fig. 3** に示すように収集データに被写体外のゼロ（既知）領域が含まれること，画像再構成マトリクスは被写体が完全に含まれるように十分に大きく設定することの 2 つの条件の下，OSEM などの逐次近似画像再構成法によって視野内は正確な値に収束する．本手法により，トランケーションがあっても定量性が確保される（**Fig. 4**）．

5. マイクロ SPECT を用いた定量的機能評価の例

1）ラット心筋血流量・血管反応性

近年高血圧や高脂血症などの循環器疾患に関与する遺伝子が明らかになってきており，疾患発現に先行する病態生理の把握が重要になる．このとき，安静時のみの組織血流量や基質代謝量に加えて，種々の生理的・薬理的な賦活に対する反応性，たとえば血管反応性や代謝自動調節能などが指標になると考えられている．

著者らは，小動物でこのような生理機能の定量評価を目的として，小型高解像度ピクセル型 NaI シンチレータとピンホールコリメータを組み合わせた検出器〔20〕を 4 台搭載した小動物専用高解像度 SPECT 装置を開発した（**Fig. 5**）．

本装置を用いて，覚醒下での健常ラットの心筋血流量および血管反応性を評価した．ラットは **Fig. 6** のように装置にセットされた．8 匹のラットを用いて ^{201}Tl を 36 分間隔で分割投与し，4 匹は安静時と安静時，残りの 4 匹は安静時と血管拡張時の心筋血流量を測定した．血管拡張時には血管拡張薬アデノシン A2A アゴニスト CGS21680 を 2 回目の ^{201}Tl 投与の 6 分前に投与した．ピンホール用 3D-OSEM で画像再構成して得られた一連の時系列画像データに対して 2 コンパートメントモデル〔21〕を適用した．**Fig. 7** は本実験で得られた心筋 SPECT 画像であるが，非常に鮮明な画像が得られた．入力関数は，別実験で 10 匹のラットの頻回採血から作成した標準入力関数を用いた．実験の結果，安静時と安静時の検査では血流値に変化はなく，安静時と負荷時の検査では血管拡張薬の量に依存して，血流上昇が認められた（**Fig. 8**）．本マイクロ SPECT システムで得られたデータを動態解析することで，小動物の心筋血流量および血管反応性を 1 回の検査で定量的に評価可能である．

2）マウス脳血流量

局所脳血流量は脳梗塞の治療効果を評価する

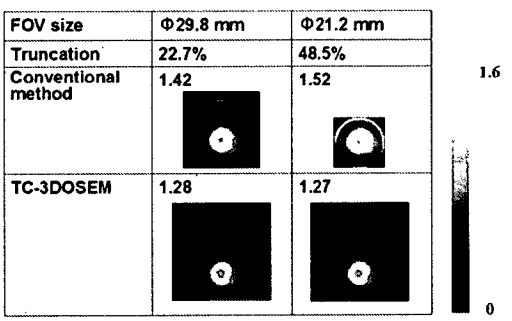

Fig. 4 Reconstructed images and myocardial counts obtained by conventional method and TC-3DOSEM. We artificially generated data with the different amount of truncation from rat experimental data. TC-3DOSEM method eliminates overestimation and provides quantitative image in independence of the amount of truncation.

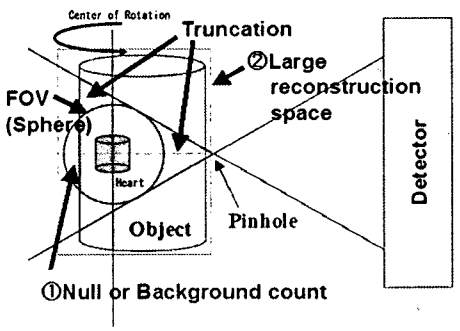

Fig. 3 Schematic diagram to show conditions for truncation compensated reconstruction in 3D pinhole SPECT.

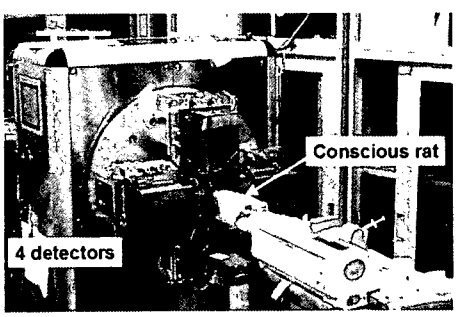

Fig. 5 Photograph of our microSPECT system and rat cardiac imaging study.

指標の1つである．6匹の脳梗塞モデルマウスを準備し，その中の3匹に対して骨髄単核球細胞を移植(治療)した．未治療群3匹と治療群3匹において，ピンホールSPECTと^{123}I-iodoamphetamine (IMP) を用いた脳組織血流定量の妥当性および移植治療効果を評価した．臨床用 SPECT 装置 (GCA-7200A, Toshiba) にピンホールコリメータを装着し，IMP 投与約 10 分後に摘出脳を回転ステージに載せ，各 1 時間 SPECT 撮像した．ピンホール用3D-OSEMで再構成して得られた画像に2コンパートメントモデル〔22〕を適用して，空間解像度 0.9 mm の 3 次元脳組織血流分布像を得た (**Fig. 9**)．入力関数は別実験で 5 匹のマウスの頻回採血によって得られた標準入力関数を利用し，分配定数は 45 ml/ml〔23〕を採用した．また，SPECT 撮像の前に MRI で T2 強調画像を得て位置合わせを行い，梗塞領域を特定した (**Fig. 9**)．得られた局所脳血流量は，正常側で 1.09 ± 0.21 ml/g/min であり，既報のノーマルマウスを 14C とオートラジオグラフィで測定した結果〔24〕の範囲であった．一方，梗塞巣で 0.76 ± 0.18 ml/g/min であり，有意に血流低下がみられた．また，未治療群と治療群の比較では，治療群で脳血流量の改善効果がみられた．ピンホール SPECT でマウス脳梗塞モデルを用いた病態の定量評価が可能である．今後，同一マウスによる in vivo 繰り返し撮像を予定している．また，^{123}I標識技術はペプチドやタンパクのイメージングを可能とし，マイクロ PET を補う技術になりうることが認められる．

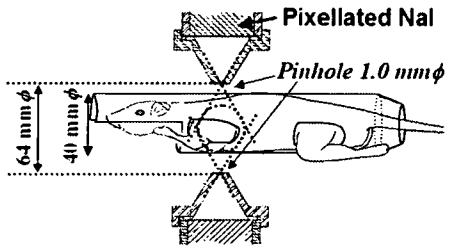

Fig. 6 Imaging geometry. Rat was set in a dedicated holder for conscious condition.

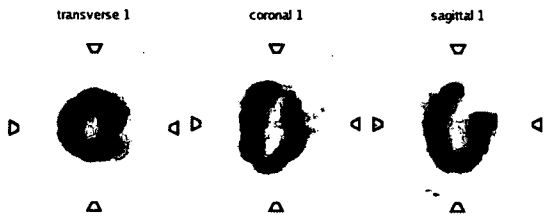

Fig. 7 Representative rat cardiac images obtained by our microSPECT and ^{201}Tl.

6. まとめ

創薬や治療法評価などの前臨床研究における小動物イメージングの定量的機能評価は重要な役割を担っている．高解像度を有するマイクロ SPECT 装置は最近の物理工学的な進歩によって小動物 PET 同様に定量解析が可能になったことと，検査の簡便さも手伝って今後広く普及するものと考えられる．

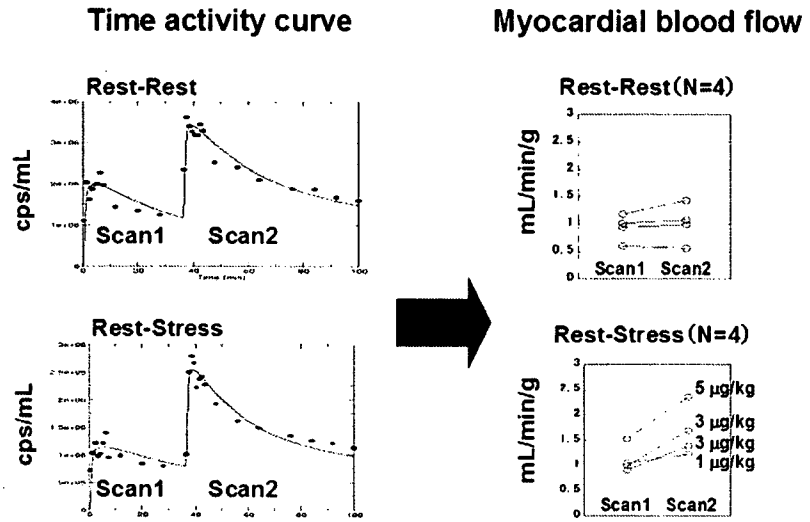

Fig. 8 Quantitaion of rat myocardial blood flow using data from microSPECT. Left: Representative time activity curves in rest-rest and rest-stress studies. Right: Myocardial blood flows calculated by two-compartment model. Coronary flow reserves were assessed in rest-stress studies.

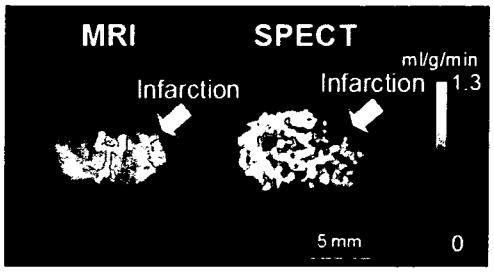

Fig. 9 Co-registrated MR and SPECT images of cerebral infraction model mouse. Left: T2 weighted image obtained by MRI. Right: Quantitative cerebral blood flow image obtained by pinhole SPECT and ^{123}I-IMP.

謝　辞

本研究の一部は，独立行政法人科学技術振興機構課題番号 1702，および厚生労働科学研究費補助金「こころの健康科学研究」により実施された．

文　献

〔1〕 Larobina M, Brunetti A, Salvatore M : Small animal PET: a review of commercially available imaging systems. Curr Med Imag Rev **2**: 187-192, 2006

〔2〕 Miekle SR, Kench P, Kassiou M et al : Small animal SPECT and its place in the matrix of molecular imaging technologies. Phys Med Biol **50**: R45-R61, 2005

〔3〕 銭谷　勉，渡部浩司，工藤博幸，他：完全データを利用したピンホール SPECT. Med Imag Tech **23**: 9-16, 2005

〔4〕 Liu Z, Kastis GA, Stevenson GD et al: Quantitative analysis of acute myocardial infarct in rat hearts with ischemia-reperfusion using a high-resolution stationary SPECT system. J Nucl Med **43**: 933-939, 2002

〔5〕 Schramm NU, Ebel G, Engeland U et al: High-resolution SPECT using multipinhole collimation. IEEE Trans Nucl Sci **50**: 315-320, 2003

〔6〕 Beekman FJ, van der Have F, Vastenhouw B et al: U-SPECT-I: a novel system for submillimeter-resolution tomography with radiolabelled molecules in mice. J Nucl Med **46**: 1194-1200, 2005

〔7〕 Zeniya T, Watabe H, Aoi T et al: A new reconstruction strategy for image improvement in pinhole SPECT. Eur J Nucl Med Mol Imaging **31**: 1166-1172, 2004

〔8〕 Watabe H, Ikoma Y, Kimura Y et al: PET kinetic analysis-compartmental model. Ann Nucl Med **20**: 583-589, 2006

〔9〕 Kudomi N, Choi E, Yamamoto S et al: Development of a GSO detector assembly for a continuous blood sampling system. IEEE Trans Nucl Sci **50**: 70-73, 2003

〔10〕 Acton PD, Choi S-R, Plōssl K et al: Quantification of dopamine transporters in the mouse brain using ultra-high resolution single-photon emission tomography. Eur J Nucl Med **29**: 691-698, 2002

〔11〕 Sohlberg A, Watabe H, Zeniya T et al: Comparison of multi-ray and point-spread function based resolution recovery methods in pinhole SPECT reconstruction. Nucl Med Commun **27**: 823-827, 2006

〔12〕 飯田秀博，渡部浩司，赤松哲哉，他：SPECT を使った脳機能画像の定量化と標準化．脳神経外科ジャーナル **16**: 742-752, 2007

〔13〕 Wang Y, Du Y, Mok SP et al: Towards quantitative high-resolution pinhole SPECT imaging. [Abstract] J Nucl Med **45**(suppl 2): 110, 2005

〔14〕 Deloar H, Watabe H, Aoi T et al: Evaluation of penetration and scattering components in conventional pinhole SPECT: phantom studies using Monte Carlo simulation. Phys Med Biol **48**: 995-1008, 2003

〔15〕 van der Have F, Beekman FJ: Penetration and scatter in channel micro-pinholes for SPECT: a Monte Carlo investigation. 2004 IEEE Nuclear Science Symposium Conference Record **4**: 2575 - 2578, 2004

〔16〕 Vanhove C, Defrise M, Franken PR et al: Interest of the ordered subsets expectation maximization (OS-EM) algorithm in pinhole single-photon emission tomography reconstruction: a phantom study. Eur J Nucl Med **27**: 140-146, 2000

〔17〕 Metzler SD, Greer KL, Jaszczak RJ: Helical pinhole SPECT for small-animal imaging: a method for addressing sampling completeness. IEEE Trans Nucl Sci **50**: 1575-1583, 2003

〔18〕 Defrise M, Noo F, Clackdoyle R et al: Truncated Hilbert transform and image reconstruction from limited tomographic data. Inverse Probl **22**: 1037-1053, 2006

〔19〕 Zeniya T, Watabe H, Sohlberg A et al: 3D-OSEM reconstruction from truncated data in pinhole SPECT. 2007 IEEE Nuclear Science Symposium Conference Record: 4205-4207, 2007

〔20〕 Zeniya T, Watabe H, Aoi T et al: Use of a compact pixellated gamma camera for small animal pinhole SPECT imaging. Ann Nucl Med **20**: 409-416, 2006

〔21〕 Iida H, Eberl S: Quantitative assessment of regional myocardial blood flow with thallium-201 and SPECT. J Nucl Cardiol **5**: 313-331, 1998

〔22〕 Iida H, Itoh H, Nakazawa M et al: Quantitative mapping of regional cerebral blood flow using iodine-123-IMP and SPECT. J Nucl Med **35**: 2019-2030, 1994

〔23〕 Iida H, Akutsu T, Endo K et al: A multicenter validation of regional cerebral blood flow quantitation using [^{123}I]iodoamphetamine and single photon emission computed tomography. J Cereb Blood Flow Metab **16**: 781-793, 1996

〔24〕 Maeda K, Mies G, Oláh L et al: Quantitative measurement of local cerebral blood flow in the anesthetized mouse using intraperitoneal [14C]iodoantipyrine injection and final arterial heart blood sampling. J Cereb Blood Flow Metab **20**: 10-14, 2000

銭谷　勉（ぜにや　つとむ）

1991 年山形大学工学部情報工学科卒業．1993 年山形大学大学院工学研究科情報工学専攻修士課程修了．同年㈱日立メディコ入社．2002 年山形大学大学院理工学研究科システム情報工学専攻博士後期課程修了．2001~2002 年日本学術振興会特別研究員．現在，国立循環器病センター研究所先進医工学センター放射線医学部特任研究員．博士（工学）．小動物 SPECT，画像再構成法の研究開発に従事．1998 年日本医用画像工学会論文賞．2005 年日本核医学会研究奨励賞．

Polymer Journal, Vol. 39, No. 10, pp. 1065–1070 (2007)

Synthesis of Sugar-Polysiloxane Hybrids Having Rigid Main-Chains and Formation of their Nano Aggregates

Koutarou BEPPU,[1] Yoshiro KANEKO,[1] Jun-ichi KADOKAWA,[1,†]
Hidezo MORI,[2] and Takehiro NISHIKAWA[2]

[1]*Department of Nano-structured & Advanced Materials, Graduate School of Science and Engineering, Kagoshima University, 1-21-40 Korimoto, Kagoshima 890-0065, Japan*
[2]*National Cardiovascular Center Research Institute, 5-7-1, Fujishirodai, Suita 565-8565, Japan*

(Received March 22, 2007; Accepted July 12, 2007; Published August 28, 2007)

ABSTRACT: We synthesized sugar-polysiloxane hybrids having rigid main-chains by reaction of sugar-lactones with amine-functionalized polysiloxane (**1**). Reaction of gluconolactone (**2**) with **1** was performed to obtain polysiloxane (**3**) having polyol moieties derived from glucose. This material has the regularly controlled higher-ordered structure in solid state such as the hexagonal phase. A hydrophilic sugar-polysiloxane hybrid (**5**) was prepared by reaction of lactobionolactone (**4**) with **1**. Furthermore, an amphiphilic sugar-polysiloxane hybrid (**8**) was synthesized by introduction of stearoyl groups in addition to sugar groups on the surface of **1**. The SEM image of the amphiphilic material **8** exhibited formation of nano aggregates having the particle diameters of *ca.* 50 nm in water.
[doi:10.1295/polymj.PJ2006268]
KEY WORDS Glycopolymer / Sugar-lactone / Polysiloxane / Amphiphilic / Hybrid / Nano Aggregate /

There has been a growing interest in sugar portions of the glycoproteins because of exhibiting to bind to carbohydrate-recognition proteins, toxins, viruses, and cells. It has been known that a molecular assembly formed from the sugar-residues in the living system expresses stronger recognition ability than that of a single sugar molecule. This, so-called multivalent or cluster effect, has become a principle in the design of artificial glycoconjugate ligands. Therefore, polymeric materials having such functional sugar-residues, *i.e.*, 'glycopolymer', have widely been investigated because these materials efficiently show the multivalent effect.[1] So far, a number of such glycopolymers have been synthesized, which are composed of various organic polymer main-chains combined with a variety of sugar side-chains.[2–6]

Inorganic polymers such as polysiloxanes have various of interesting properties, *e.g.*, high oxygen permeability, low toxicity, and biocompatibility, which are advantages as biomaterials. Therefore, sugar-polysiloxane hybrids would be expected to have a significant potential for biological applications. In previous study, synthesis of such sugar-inorganic hybrids, composed of polydimethylsiloxane main-chain has been reported.[7–10] Since the main-chain has relatively flexible nature, nanostructures of the hybrid materials have not been controlled well.

Based on the above viewpoints, we paid attention to amine-functionalized polysiloxanes[11,12] for the main-chain of new sugar-polysiloxane hybrids, which were prepared by sol-gel reaction of amine-functionalized organoalkoxysilanes in strong acid aqueous solutions. The materials have rigid structures and construct hexagonal phase in solid state, because their frameworks are Si-O-Si network structures derived from trifunctional organoalkoxysilane. Furthermore, the materials are soluble in water and have reactive amino groups on the surface. Their rigidity, solubility, and reactivity would be advantageous properties to controlling nanostructures and introduction of various functional groups on the surface, in addition to the general characteristics of the inorganic polymers.

In previous communication, we briefly reported simple preparation method for a rigid polysiloxane hybrid (**3**) having polyol moieties using the amine-functionalized polysiloxane (**1**) and gluconolactone (**2**) (Scheme 1).[13] Because the sugar lactones like **2** react with the amino groups without protection of the hydroxy groups, they are useful substrates for such the simple procedure to exclude multi-reaction steps. However, **2** was not suitable for preparation of materials containing the sugar substituents, because the ring-opened moieties like the side chain of **3** formed from **2** had no any sugar-residues. Therefore, we have been carrying out studies on the synthesis of sugar-functionalized polysiloxane hybrids using disaccharide-lactone such as lactobionolactone (**4**), because the existence of sugar-residues can be maintained in spite of opening the lactone ring of **4** by the reaction with **1**.

†To whom correspondence should be addressed (Tel: +81-99-285-7743, Fax: +81-99-285-3253, E-mail: kadokawa@eng.kagoshima-u.ac.jp).

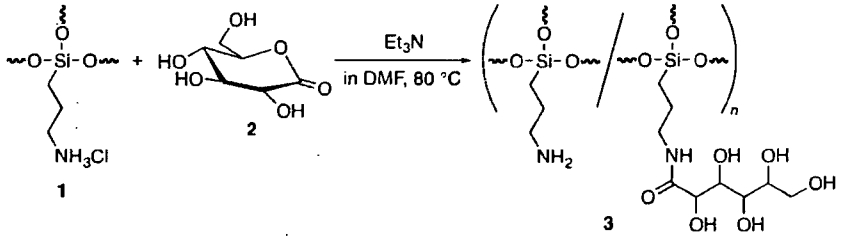

Scheme 1.

In this paper, we describe the synthesis of sugar-polysiloxane hybrids having rigid main-chains by the reaction of sugar-lactones with **1**. Furthermore, we prepared an amphiphilic sugar-polysiloxane hybrid by introduction of long alkyl chains in addition to sugar-residues on the surface of **1** to promote the formation of the nano aggregates in water, expecting the multivalent effects.

EXPERIMENTAL

Materials

The polysiloxane **1** was prepared according to the literature procedure.[11] *N,N*-Dimethylformamide (DMF), dimethyl sulfoxide (DMSO), and triethylamine were purified by distillation. Other reagents were used as received.

Reaction of 1 with Gluconolactone 2[13]

To a suspension of **1** (0.147 g, 1.0 mmol unit) in DMF (2.5 mL) was successively added triethylamine (0.15 mL, 1.1 mmol) and a solution of **2** (0.891 g, 5.0 mmol) in DMF (10 mL) with vigorously stirring at 80 °C under argon. After the mixture was stirred further at that temperature for 13 h, the obtained product was isolated by filtration, washed with DMF and acetone, and then dried under reduced pressure at 40 °C to yield 0.191 g of the yellow-powdered **3**. ^{1}H NMR (600 MHz, D_2O): δ 4.38–4.26 (br, -C(=O)-C*H*-), δ 4.16–4.05 (br, -C(=O)CH(OH)C*H*-), δ 3.88–3.60 (br, -C*H*(OH)C*H*(OH)CH_2-), δ 3.41–3.10 and 3.06–2.91 (br, -NCH_2-), δ 1.88–1.45 (br, -NCH$_2$CH_2-CH$_2$Si-), δ 0.94–0.47 (br, -CH_2Si-).

Synthesis of Hydrophilic Sugar-Polysiloxane Hybrid (5)

To a suspension of **1** (0.147 g, 1.0 mmol unit) in DMSO (3.0 mL) was successively added triethylamine (0.34 mL, 2.4 mmol) and a solution of **4** (1.701 g, 5.0 mmol) in DMSO (10 mL) with vigorously stirring at 80 °C under argon, and the mixture was stirred further at that temperature for 2 h. The mixture became gradually homogeneous solution. The solution was poured into acetone (300 mL) to precipitate the powdered product. The precipitated product was isolated by filtration, successively washed with acetone, hydrochloric acid (HCl) methanol solution and methanol, and then dried under reduced pressure at 40 °C to yield 0.332 g of the light yellow-powdered **5**. ^{1}H NMR (600 MHz, D_2O): δ 4.65–4.50 (br, -OC*H*-(CH-)O-), δ 4.50–4.32 (br, -C(=O)C*H*(OH)-), δ 4.32–4.13 (br, -C(=O)CH(OH)C*H*(OH)-), δ 4.08–3.49 (br, -C*H*(O-)C*H*(OH)CH_2OH, -C*H*(OH)C*H*(OH)C*H*(OH)-C*H*(O-)CH_2OH), δ 3.40–3.12 (br, -C(=O)NHCH_2-), δ 3.12–2.87 (br, Cl·NH$_3$CH_2-), δ 1.95–1.43 (br, -NCH$_2$CH_2CH$_2$Si-), δ 0.93–0.50 (br, -CH_2Si-).

Synthesis of Stearoyl-Carrying Polysiloxane (7)

To a solution of **1** (0.440 g, 3.0 mmol unit) in water (10 mL) was successively added triethylamine (1.0 mL, 7.2 mmol) and a solution of stearoyl chloride (**6**) (0.182 g, 0.6 mmol) in DMF (30 mL) with vigorously stirring at room temperature, and the solution was stirred further at that temperature for 10 min. After 5 mol/L HCl aqueous solution (2.88 mL, 14.4 mmol) was added to this mixture and this solution was stirred further for 5 min, the solution was poured into acetone (300 mL) to precipitate the powdered product. The precipitated product was isolated by filtration, washed with acetone and chloroform, and then dried under reduced pressure at 40 °C to yield 0.437 g of the white-powdered **7**. ^{1}H NMR (600 MHz, DMSO-d_6-D_2O): δ 3.09–2.72 (br, -NCH_2-), δ 2.20–2.01 (br, -C(=O)CH_2-), δ 1.88–1.55 (br, -NCH$_2$CH_2-CH$_2$Si-), δ 1.50–1.40 (br, -C(=O)CH$_2$CH_2-), δ 1.28–1.10 (br, -CCH_2C-), δ 0.95–0.45 (br, -CH$_3$, -CH_2Si-).

Synthesis of Amphiphilic Sugar-Polysiloxane Hybrid (8)

To a solution of **7** (0.150 g, 1.3 mmol unit) in DMSO (5 mL) was successively added triethylamine (0.46 mL, 3.3 mmol) and a solution of **4** (2.212 g, 6.5 mmol) in DMSO (15 mL) with stirring at 80 °C, and the solution was stirred further at that temperature for 2 h. The solution was poured into acetone (300 mL) to precipitate the powdered product. The precipitated product was isolated by filtration, successively washed with acetone, HCl methanol solution and

methanol, and then dried under reduced pressure at 40 °C to yield 0.270 g of the light yellow-powdered **8**. ^{1}H NMR (600 MHz, DMSO-d_6-D_2O): δ 4.46–4.28 (br, -OC*H*(CH-)O-), δ 4.28–4.11 (br, -C(=O)C*H*-(OH)-), δ 4.11–3.95 (br, -C(=O)CH(OH)C*H*(OH)-), δ 3.90–3.28 (br, -C*H*(O-)C*H*(OH)CH_2OH, -C*H*(OH)-C*H*(OH)C*H*(OH)C*H*(O-)CH_2OH, overlapped with HOD signal), δ 3.28–2.96 (br, -C(=O)NHCH_2-), δ 2.96–2.70 (br, Cl·NH_3CH_2-), δ 2.20–2.01 (br, -C(=O)-CH_2-), δ 1.80–1.32 (br, -NCH_2CH_2CH_2Si-, -C(=O)-CH_2CH_2-), δ 1.28–1.13 (br, -CCH_2C-), δ 0.88–0.80 (br, -CH_3), δ 0.80–0.36 (br, -CH_2Si-).

Measurements

The IR spectra were recorded using a SHIMADZU FT/IR-8400 spectrometer. The ^{1}H NMR spectra (600 MHz) were recorded using a JEOL ECA600 spectrometer. The gel permeation chromatographic (GPC) analyses were performed by using a TOSOH CCPD with RI detector under the following conditions: Shodex GF-310 column with water as the eluent at a flow rate of 0.5 mL/min. The calibration curve was obtained using pullulan standards. The X-ray diffraction (XRD) measurements were conducted at a scanning speed of $2\theta = 0.2°$/min using a RINT 1200 (Rigaku Co., Ltd) diffractometer with Ni-filtered CuKα radiation ($\lambda = 0.15418$ nm). The scanning electron microscope (SEM) images were obtained using a Hitachi S-4100 electron microscope. The dynamic light scattering (DLS) measurement was performed on a Zetasizer 3000 (Malvern Instruments).

RESULTS AND DISCUSSION

Reaction of 1 with 2

As previously reported,[13] an introduction of **2** to **1** was performed by heating at 80 °C in the presence of triethylamine in DMF to prepare a rigid polysiloxane **3** having polyol moieties (Scheme 1). The obtained product **3** was soluble in water and DMSO, but insoluble in typical organic solvents such as methanol, acetone, chloroform, and *n*-hexane.

The IR spectrum of the product showed an absorption at 1150 cm^{-1} attributed to the Si-O bond of the polysiloxane, an absorption at 1080 cm^{-1} assigned to the C-O bond of the polyol moiety derived from **2**, and an absorption at 1650 cm^{-1} due to the C=O bond of the amido group. In addition, the ^{1}H NMR spectrum in D_2O of the product showed both signals due to **1** and **2**. Furthermore, a methylene signal (δ 3.41–3.10) neighboring the amido group was appeared at lower magnetic field compared with a signal (δ 3.06–2.91) neighboring the unreacted amino group. These spectroscopic results indicated that the product has the structure **3** connecting **1** with **2** by the covalent bonds. The functionality of **2** to **1** was calculated to be *ca.* 75% based on the integrated ratio of the methylene signal neighboring the amido group to the methylene signal neighboring the silicon atom.

The molecular weights of **3** and **1** were evaluated by GPC analyses with water as the eluent. The GPC peak of **3** was shifted to the range of higher molecular weight compared to that of **1**. The M_n values of **3** and **1** estimated using pullulan standards were 21,200 g/mol ($M_w/M_n = 1.33$) and 10,300 g/mol ($M_w/M_n = 1.41$), respectively.

The XRD profile of **3** showed three peaks with the *d*-value ratio of $1:1/\sqrt{3}:1/2$ assigned to the (100), (110), and (200) peaks, respectively, indicating that the product has a hexagonal phase. Additionally, the *d*-value of the (100) peak of **3** ($d = 1.76$ nm) was larger than that of **1** ($d = 1.41$ nm). This indicates that the hexagonal phase in solid state was maintained in spite of the increase in the *d*-value by introduction of **2** to **1**.

The above analytical data indicated that **2** efficiently reacted with the amino groups in **1**, giving rise to **3**. To introduce the sugar moieties such as galactose residues on the surface of **1** by means of this reaction manner, the following experiments were performed using lactobionolactone **4**.

Synthesis of Hydrophilic Sugar-Polysiloxane Hybrid 5

We investigated synthesis of galactose-functionalized polysiloxane hybrid **5** by the reaction of **4** with **1**. Procedures for synthesis of **5** were almost same as those of **3**. Since the reaction in DMF gave the insoluble product, however, we employed DMSO as the alternative solvent, which was favorable for this reaction system. When an introduction of **4** to **1** was performed by heating at 80 °C in the presence of triethylamine in DMSO (Scheme 2), the initial reaction system was heterogeneous, which gradually became homogeneous with progress of the reaction. After the product was isolated as the fraction insoluble in acetone, unreacted amino groups were converted to ammonium cations by addition of HCl methanol solution in order to increase solubility and stability of the product in water. The obtained product **5** was soluble in water and DMSO, but insoluble in typical organic solvents such as methanol, acetone, chloroform, and *n*-hexane.

The IR spectrum of the product showed absorptions at 1650 cm^{-1} attributed to the C=O bond of the amido group, indicating the introduction of **4** to **1**. The ^{1}H NMR spectrum in D_2O of the product in Figure 1 shows both signals derived from **1** and **4**. Furthermore, a methylene signal $\mathbf{H_c}$ neighboring the amido group appeared at lower magnetic field compared with a signal $\mathbf{H_{c'}}$ neighboring the unreacted amino group. These spectroscopic data support the structure **5** of

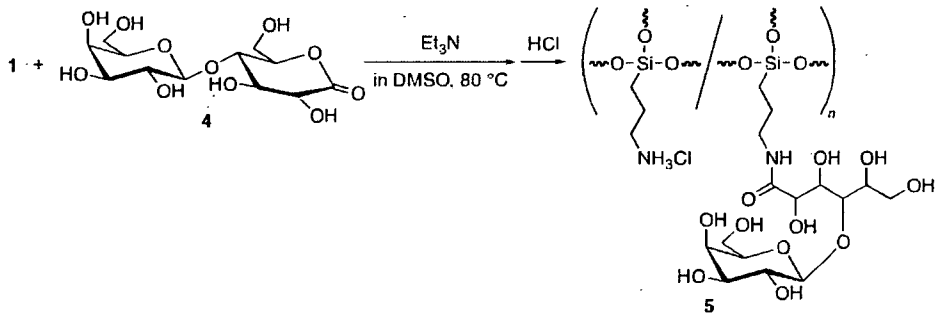

Scheme 2.

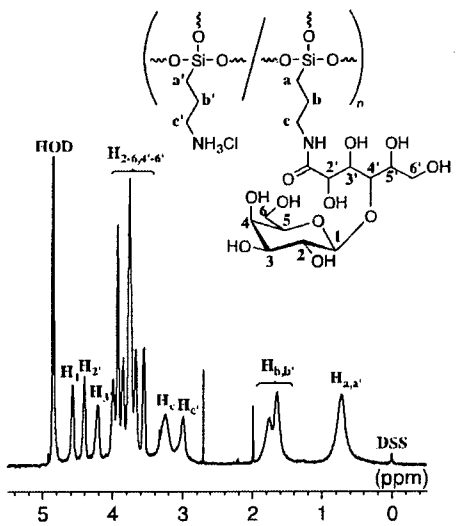

Figure 1. ^{1}H NMR spectrum of **5** in D_2O. Chemical shifts were referenced to sodium 2,2-dimethyl-2-silapentane-5-sulfonate (DSS) (δ 0.0 ppm).

the product. The functionality of **4** to **1** was calculated by the integrated ratio of the signal $\mathbf{H_1}$ to the signals $\mathbf{H_a}$ and $\mathbf{H_{a'}}$ in Figure 1 to be *ca.* 57%. Although the XRD profile of **3** showed three peaks for a typical hexagonal phase as described above, no diffraction peak was observed for **5**, indicating that a regular higher-ordered structure was not formed in the solid state. This would be because that the bulkiness of **4** affected the higher-ordered structure of **5**. However, **5** probably has the rigid structure in the solution due to the Si-O-Si network structure of the main-chain derived from trifunctional organoalkoxysilane. The molecular weight (M_n) of **5** estimated by GPC analysis with water as the eluent using pullulan standards was 44,700 g/mol ($M_w/M_n = 1.44$).

Synthesis of Amphiphilic Sugar-Polysiloxane Hybrid 8

To promote the formation of the nano aggregates of sugar-polysiloxane hybrid, we attempted synthesis of an amphiphilic hybrid **8** by introduction of the hydrophobic stearoyl groups in addition to the hydrophilic sugar groups on the surface of **5**. However, the reaction of **5** with stearoyl chloride **6** did not proceed to obtain **8**, probably due to bulkiness of sugar-residues existed on the surface of **5**. As an alternative reaction manner, an introduction of **6** to **1** was firstly carried out in the presence of triethylamine in water/DMF mixed solvent at room temperature to produce stearoyl-carrying polysiloxane **7** (Scheme 3). After addition of HCl aqueous solution to this reaction solution, the product was isolated as the fraction insoluble in acetone. The obtained product **7** was soluble in DMSO, but insoluble in water.

The IR spectrum of the product showed an absorption at 1640 cm^{-1} assigned to the C=O bond of the amido group. In addition, the ^{1}H NMR spectrum in DMSO-d_6 (including a small amount of D_2O) of the product in Figure 2 shows both signals derived from **1** and **6**. These spectroscopic results indicate the intro-

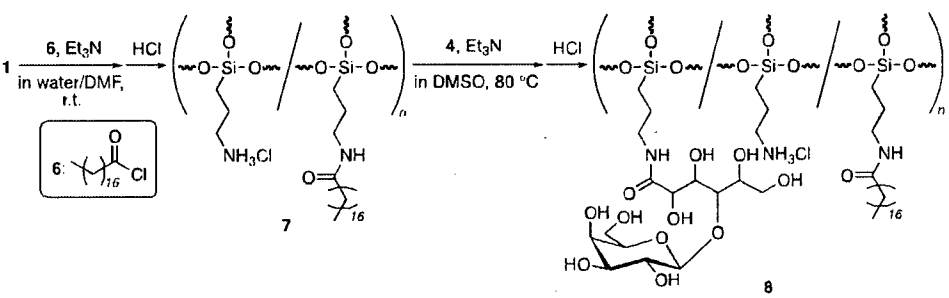

Scheme 3.

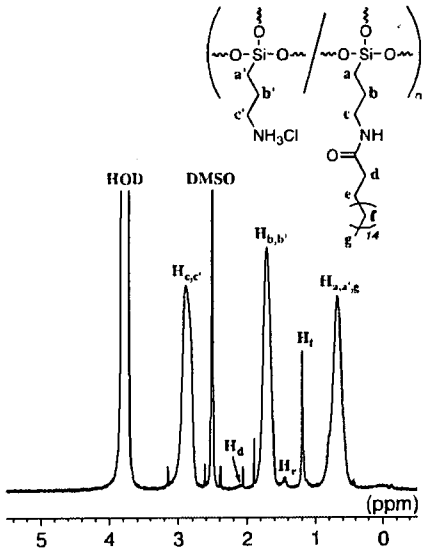

Figure 2. ^{1}H NMR spectrum of **7** in DMSO-d_6 (including a small amount of D_2O). Chemical shifts were referenced to DMSO (δ 2.5 ppm).

duction of **6** to **1**, leading to **7**. The functionality of **6** to **1** was calculated to be *ca.* 2% based on the integrated ratio of the signal $\mathbf{H_f}$ to the signal $\mathbf{H_b}$ and $\mathbf{H_{b'}}$. When the feed ratio of **6** to **1** was increased, the insoluble product was obtained.

As a second step, we carried out a reaction of **4** with **7** by heating at 80 °C in the presence of triethylamine in DMSO to obtain amphiphilic sugar-polysiloxane hybrid **8** (Scheme 3). The product was isolated as the fraction insoluble in acetone, followed by washing with acetone, HCl methanol solution, and methanol. The obtained product **8** was soluble in water and DMSO, but insoluble in typical organic solvents such as methanol, acetone, chloroform, and *n*-hexane.

The IR spectrum of the product showed an absorption at 1140 cm^{-1} attributed to the Si-O bond, an absorption at 1080 cm^{-1} assigned to the C-O bond of **4**, and an absorption at 1650 cm^{-1} due to the C=O bond of the amido group. Additionally, the ^{1}H NMR spectrum in DMSO-d_6 (including a small amount of D_2O) of the product in Figure 3a shows signals derived from **1**, **4**, and **6**. Furthermore, the methylene signals $\mathbf{H_a}$ and $\mathbf{H_b}$ of the product shift to higher field and the methylene signal $\mathbf{H_c}$ shifts to lower field compared with those of **7**. These shifts have also been observed in the synthesis of **3**,[13] and are attributed to progress of the amidation reaction of **7** with **4**. These spectroscopic results fully support the structure of the sugar- and stearoyl-functionalized polysiloxane **8**. The functionality of **4** to **1** was calculated by the integrated ratio of the signal $\mathbf{H_{f'}}$ to the signal $\mathbf{H_1}$ in Figure 3 to be *ca.* 48%, when the reaction was carried out under the conditions as described in experimental sec-

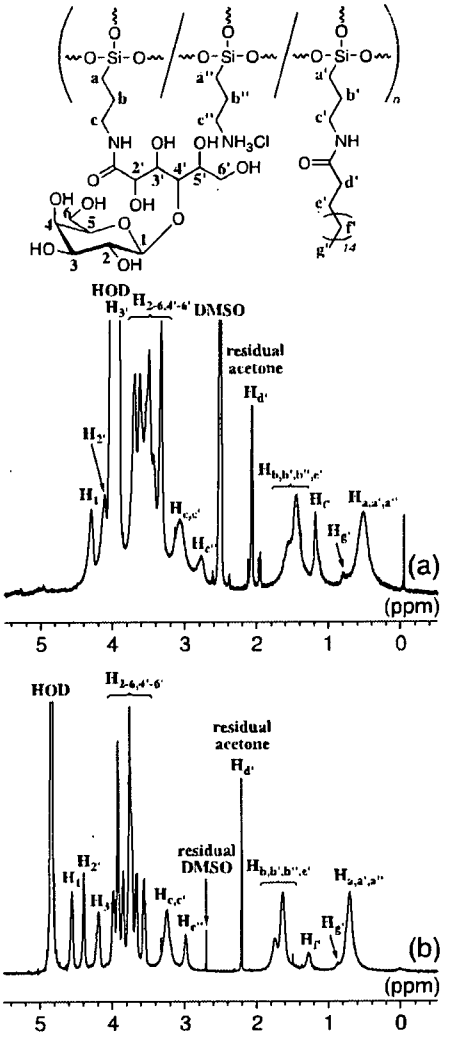

Figure 3. ^{1}H NMR spectrum of **8** (a) in DMSO-d_6 (including a small amount of D_2O) and (b) in D_2O. Chemical shifts were referenced to DMSO (δ 2.5 ppm) and DSS (δ 0.0 ppm), respectively.

tion. The functionalities were variable by changing the feed ratio of **4** to **7**.

Interestingly, intensity of a signal $\mathbf{H_{f'}}$ due to stearoyl group of **8** in D_2O decreases compared with that in DMSO-d_6 (Figure 3b). This observation indicates that the stearoyl groups existed in the inside of the intra and intermolecular aggregates of **8** in D_2O. To confirm the formation of nano aggregates of **8** in water, SEM image of **8** was taken. The SEM specimen was prepared by evaporating an aqueous solution of **8** on a spinning aluminium plate. The SEM image of the surface of **8** coated on the aluminum plate shows that nano aggregates were formed from **8** (Figure 4); nano aggregates having the particle diameters of *ca.* 50 nm are appearing at high frequency and larger particles that represent a diameter of *ca.* 500 nm are coexisting with smaller aggregates at much lower frequency (a few aggregates in a SEM image). The particle size

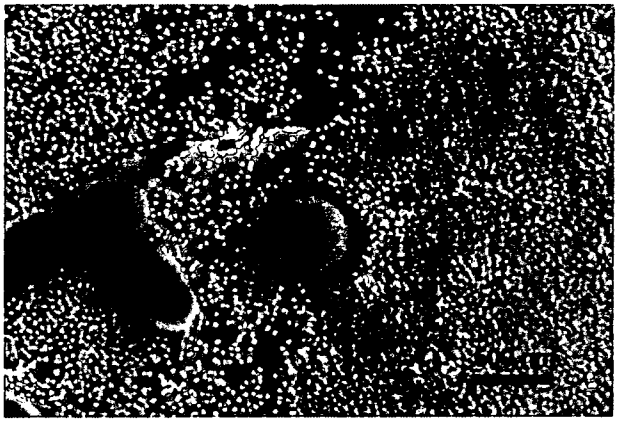

Figure 4. SEM image of **8**.

was also confirmed by dynamic light scattering (DLS) measurement. The mean diameter of the particle composed of **8** was 67.7 ± 4.5 nm (poly dispersity index: 0.273) in water. The aggregate size corresponds well to that was observed in the SEM image of the spin-coating sample of **8**.

CONCLUSIONS

The amino groups existed on the surface of the rigid polysiloxane (**1**) efficiently reacted with gluconolactone (**2**) to give the corresponding hybrid (**3**). This reaction manner was employed for preparation of the hydrophilic sugar-polysiloxane hybrid (**5**), which was achieved by the reaction of **1** with lactobionolactone (**4**). Furthermore, the amphiphilic sugar-polysiloxane hybrid (**8**) was also derived from **1** by the successive reactions with stearoyl chloride (**6**) and with **4**. The obtained hybrid materials **5** and **8** have galactose residues on their surfaces. Although hybrid **3** had the regular higher-ordered structure in the solid state, hydrophilic sugar-polysiloxane hybrid **5** did not form such a structure by the bulkiness of **4**. However, amphiphilic sugar-polysiloxane hybrid **8** formed the nano aggregates in water, which was confirmed by the ^{1}H NMR, SEM, and DLS analyses, expecting the multivalent effects of sugar-residues. The present materials are new class of sugar-inorganic hybrids, which have rigid polysiloxane main-chains.

Acknowledgment. The author (T.N.) thanks Dr. Tetsuji Yamaoka and Dr. Atsushi Mahara of National Cardiovascular Center for dynamic light scattering measurement.

REFERENCES

1. M. Okada, *Prog. Polym. Sci.*, **26**, 67 (2001).
2. K. Kobayashi, A. Tsuchida, T. Usui, and T. Akaike, *Macromolecules*, **30**, 2016 (1997).
3. X. L. Sun, K. M. Faucher, M. Houston, D. Grande, and E. L. Chaikof, *J. Am. Chem. Soc.*, **124**, 7258 (2002).
4. Q. Wang, J. S. Dordick, and R. J. Linhardt, *Chem. Mater.*, **14**, 3232 (2002).
5. A. B. Lowe, B. S. Sumerlin, and C. L. McCormick, *Polymer*, **44**, 6761 (2003).
6. L. Albertin, M. Stenzel, C. Barner-Kowollik, L. J. R. Foster, and T. P. Davis, *Macromolecules*, **37**, 7530 (2004).
7. G. Jonas and R. Stadler, *Acta. Polym.*, **45**, 14 (1994).
8. V. Braunmühl, G. Jonas, and R. Stadler, *Macromolecules*, **28**, 17 (1995).
9. V. Braunmühl and R. Stadler, *Polymer*, **39**, 1617 (1998).
10. K. Loos, G. Jonas, and R. Stadler, *Macromol. Chem. Phys.*, **202**, 3210 (2001).
11. Y. Kaneko, N. Iyi, K. Kurashima, T. Matsumoto, T. Fujita, and K. Kitamura, *Chem. Mater.*, **16**, 3417 (2004).
12. Y. Kaneko, N. Iyi, T. Matsumoto, and K. Kitamura, *Polymer*, **46**, 1828 (2005).
13. Y. Kaneko, J. Kadokawa, M. Setoguchi, and N. Iyi, *Polymer*, **46**, 8905 (2005).

ELSEVIER

Nutrition 23 (2007) 81–86

NUTRITION

www.elsevier.com/locate/nut

Basic nutritional investigation

Kurozu moromimatsu inhibits tumor growth of Lovo cells in a mouse model in vivo

Naoto Fukuyama, M.D., Ph.D.[a,*], Shio Jujo[a], Isao Ito, M.D., Ph.D.[b], Toru Shizuma, M.D., Ph.D.[a], Kazunori Myojin, M.D., Ph.D.[c], Kazuo Ishiwata, Ph.D.[a], Masanobu Nagano, Ph.D.[d], Hiroe Nakazawa, M.D., Ph.D.[a], and Hidezo Mori, M.D., Ph.D.[e]

[a] *Department of Physiology, Tokai University, School of Medicine, Isehara, Kanagawa, Japan*
[b] *Department of Surgery, Tokai University, School of Medicine, Isehara, Kanagawa, Japan*
[c] *Department of Radiology, Tokai University, School of Medicine, Isehara, Kanagawa, Japan*
[d] *Sakamoto Jozo Inc., Kagoshima, Kagoshima, Japan*
[e] *Department of Cardiac Physiology, National Cardiovascular Center, Suita, Osaka, Japan*

Manuscript received June 2, 2006; accepted October 12, 2006.

Abstract

Objective: In Japan, rice vinegar that has been matured and fermented for years in earthenware jars is considered a health food with anticolon cancer action. It is divided into the liquid component (Kurozu) and the sediment (Kurozu moromimatsu), which contains large amounts of organic materials and minerals. The effect of Kurozu moromimatsu (Kurozu-M) on cancer has not yet been examined. In this study, we examined the activity of Kurozu-M on colon cancer and investigated the mechanisms involved, focusing on active oxygen generation, apoptosis, and metalloproteinases (MMPs).

Methods: We used Lovo cells transplanted into nude mice as an experimental model. We measured the tumor volume and MMP levels and conducted hematoxylin-eosin staining (for polymorphonuclear leukocytes), terminal deoxynucleotidyl transferase-mediated dUTP nick end-labeling staining (for apoptosis), and immunostaining for nitrotyrosine (a marker of active oxygen generation) in control, Kurozu-treated, and Kurozu-M—treated groups.

Results: The tumor volume was the same in the control group (231 ± 36 mm^3) and Kurozu group (238 ± 52 mm^3), but was significantly reduced in the Kurozu-M group (152 ± 28 mm^3, $P < 0.001$ versus control). Apoptosis of tumor cells and accumulation of polymorphonuclear leukocytes were not observed. Nitrotyrosine production, total MMP levels, and MMP activation were significantly reduced in the Kurozu-M group.

Conclusion: The administration of Kurozu-M prolonged the lifespan of cancer cell–transplanted mice, inhibited tumor progression, and reduced nitrotyrosine production and MMP activation, but did not induce apoptosis.

Keywords: Kurozu; Kurozu moromimatsu; Lovo cell; Colon cancer

This work was supported by grants from Tokai University School of Medicine Research Aid in 2004, 2005, and 2006; the research and study program of Tokai University Educational System General Research Organization; the Kanagawa Nanbyou Foundation in 2004; Grants-in-Aid for Scientific Research in 2003 (grant 15659285), 2005 (grant 17659375), and 2006 (grant 18390336) from the Ministry of Education, Science and Culture, Japan; Health and Labour Sciences Research Grants for Research on Human Genome, Tissue Engineering Food Biotechnology in 2003 (grant H15-saisei-003); Health and Labour Sciences Research Grants for Comprehensive Research on Cardiovascular Diseases in 2004 (grant H16-jyunkannki[seishuu]-009) and 2006 (grant H18-jyunkannki[seishuu]-ippan-018); and Health and Labour Science Research Grants for research on medical devices for analyzing, supporting, and substituting the function of human body in 2005 (grant H17-physi-002).

* Corresponding author. Tel.: +81-463-931-121; fax: +81-463-936-684.
E-mail address: fukuyama@is.icc.u-tokai.ac.jp (N. Fukuyama).

0899-9007/07/$ – see front matter
doi:10.1016/j.nut.2006.10.004

Introduction

In Japan, rice vinegar is widely used in the preparation of Sushi or Kaisekiryouri. It is known to have a bactericidal action and an orexigenic action and was reported to have a preventive effect against hypertension and arterial sclerosis [1]. Recently, rice vinegar that has been matured and fermented for many years in earthenware jars has attracted attention as a health food. The supernatant is known as Korozu, and the solid residue of the production process, Kurozu moromimatsu (Kurozu-M), is rich in organic materials and minerals. However, the effect of Kurozu-M on disease has not yet been examined.

Colorectal cancer accounts for >90% of malignant tumors of the large intestine and is the third most common cause of death from malignant disease in the Western world [2]. It was reported that ethyl acetate extract of Kurozu inhibited carcinogenesis in azoxymethane-treated rats [3] and caused G0/G1 arrest through p21 induction in Caco-2 cells [4]. It is known that active oxygen species activate metalloproteinases (MMPs) in colon cancer tissue, leading to destruction of the basal membrane [5], thereby promoting distant metastasis. However, the effects of Kurozu on active oxygen production and MMP activation are unknown.

In this study, we examined the direct effects of Kurozu and Kurozu-M on human colon cancer cells (DLD cells, well-differentiated adenocarcinoma; Lovo cells, poorly differentiated adenocarcinoma) transplanted into nude mice and found that both inhibited tumor growth. We also examined the mechanisms involved, focusing on active oxygen production and MMP activation. Because direct measurement of active oxygen production in tissues is difficult, we used an indirect method based on staining for nitrotyrosine, the formation of which involves active oxygen.

Materials and methods

Preparation of Kurozu and Kurozu-M diets

The Kurozu and Kurozu-M diets were obtained from Sakamotojyozo Co., Ltd. (Kagoshima, Japan). The Kurozu diet included 0.32% 10-fold–concentrated Kurozu, and the Kurozu-M diet included 2% Kurozu moromimatsu powder in CE-2 basic rodent diet (Nihon CLEA Co., Ltd, Tokyo, Japan).

Preparation of animal model

Lovo and DLD cells were maintained under the conditions recommended by the supplier. Four-week-old to 6-wk-old female nude mice were maintained in a pathogen-free environment and handled according to the university's guidelines for animal care and use.

Female nu/nu mice were injected with 1×10^6 Lovo cells or DLD cells into the right flank. The tumors reached 5–10 mm in diameter at about 6 wk after injection in the control group on a standard CE-2 diet. The CE-2, Kurozu, or Kurozu-M diet was supplied from 1 wk before cancer cell injection.

Measurement of subcutaneous tumor

Tumor dimensions were measured with a linear caliper every 2 or 3 days for one month. We measured the major axis and the tumor volume, which was calculated using the equation $V\ (mm^3) = a \times b^2$, where a is the largest dimension and and b is the perpendicular diameter.

Hematoxylin-eosin staining, terminal deoxynucleotidyl transferase-mediated dUTP nick end-labeling staining, and nitrotyrosine immunostaining

At the end of the experiment, tumor tissue was fixed with 4% paraformaldehyde and sectioned. Hematoxylin-eosin (HE) staining was performed with conventional methods. Terminal deoxynucleotidyl transferase-mediated dUTP nick end-labeling (TUNEL) staining was performed according to the kit manufacturer's instructions, and apoptosis was visualized as brown staining, located in the nucleus. Apoptotic cells were counted in 10 fields of each slide under a 40× microscope.

For nitrotyrosine staining, endogenous peroxidase in sections was quenched with 0.3% H_2O_2 in 60% methanol for 30 min. The sections were permeabilized with 0.1% Triton X-100 in phosphate buffered saline (PBS) for 20 min. Nonspecific adsorption was minimized by incubating the sections in 2% normal goat serum in PBS for 20 min. Sections were incubated overnight with anti-nitrotyrosine rabbit polyclonal antibody (1:500 in PBS), and specific labeling was detected with diaminobenzidine tetrahydrochloride. To verify the binding specificity to nitrotyrosine, some sections were incubated with primary antibody only (no secondary antibody) or with secondary antibody only (no primary antibody). No positive staining was found in these sections, indicating that the immunoreaction was specific. Some sections were incubated with the primary antibody (anti-nitrotyrosine) in the presence of excess nitrotyrosine (10 mM) to further verify the binding specificity.

MMP-2 and MMP-9 assays

Levels of total MMP-2 and MMP-9 and endogenous activated MMP-2 and MMP-9 were assayed with commercial assay kits (Amersham Pharmacia Biotech, Buckinghamshire, UK).

MMP-2 assay

Eight weeks after injection of Lovo cells, tumors were removed. Tissues were homogenized in 50 mM Tris-HCl buffer (pH 7.4) containing 1 mM monothioglycerol and

centrifuged at 2000 *g* for 10 min. The supernatant was used as the sample. One hundred microliters of each standard blank or sample (in duplicate) was added to wells coated with MMP-2 antibody. The 96-well plate was then incubated overnight at 4°C. Any MMP-2 present within the samples was bound to the wells and other components were removed by washing. All standards and one well for each sample were activated with aminophenylmercuric acetate (APMA, 0.5 mM) to determine total MMP-2 levels, and the remaining wells were incubated with assay buffer alone to determine endogenous activated MMP-2. The detection reagent was then added to each well and the plate was incubated at 37°C for 4 h. After incubation, the absorbance of each well was read at 405 nm on a microplate reader and the concentrations (nanograms per milliliter) of total MMP-2 and endogenous activated MMP-2 were determined for each sample from a standard curve using Revelation Software (Dynatech, UK). Final tissue values were expressed as nanograms per milligram of protein.

MMP-9 assay

Standards and samples were run in the same manner as described for MMP-2 on a microplate coated with MMP-9 antibody, except that 1 mM APMA was used for activation, and incubation with the detection reagent was done at 37°C for 6 h. The absorbance was read with a microplate reader as described for MMP-2. Final tissue values were expressed as nanograms per milligram of protein.

Results

Measurement of subcutaneous tumor

We measured the major axis of the tumor to examine whether the administration of Kurozu or Kurozu-M could inhibit tumor growth. In the DLD cell–transplanted model, the major axes were 8.1 ± 0.5 mm in the control group, 7.90 ± 0.80 mm in Kurozu group, and 7.8 ± 0.80 mm in the Kurozu-M group. There were no significant differences among the three groups (Fig. 1A). However, in the Lovo cell–transplanted model, the major axes of the tumor were 8.2 ± 0.5 mm in the control group and 7.8 ± 0.8 mm in the Kurozu group, but significantly reduced to 6.0 ± 0.8 mm in the Kurozu-M group ($P < 0.05$ versus control; Fig. 1B).

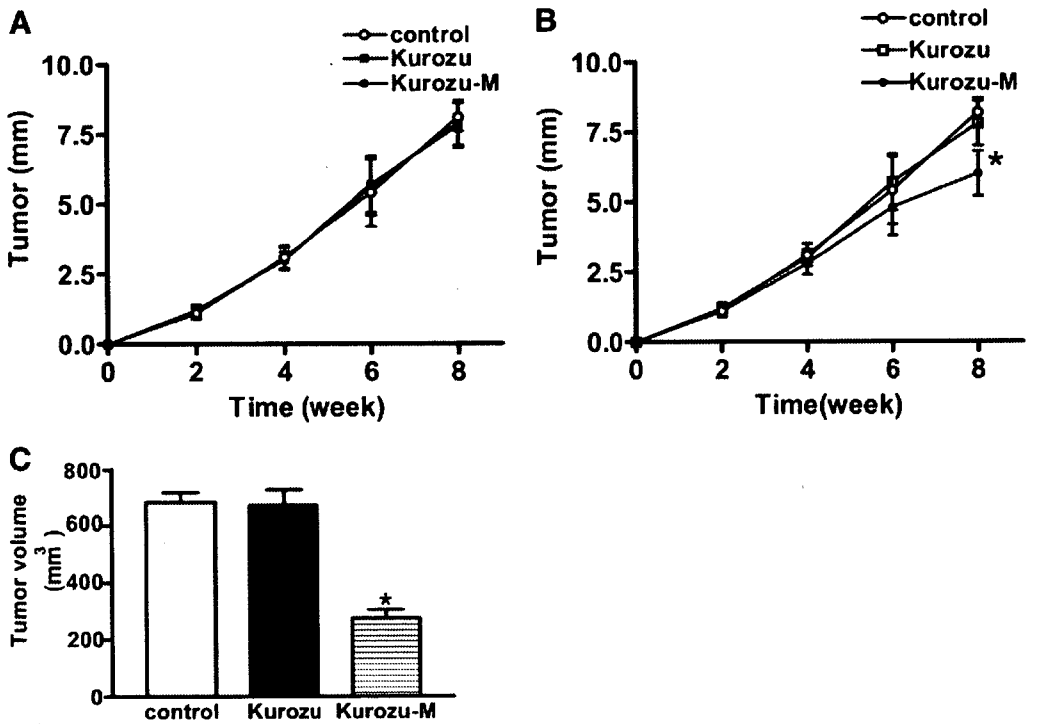

Fig. 1. Antitumor effect of Kurozu and Kurozu moromimatsu. Female nu/nu mice were injected with 1×10^6 Lovo cells or DLD cells into the right flank. (A) Time course of tumor growth in DLD-1 cell–transplanted mice (long diameter). Open circles represent the control group, solid squares the Kurozu-treated group, and solid circles the Kurozu moromimatsu–treated group. (B) Time course of tumor growth in Lovo cell–transplanted mice (long diameter). Open circles indicate the control group, open squares the Kurozu-treated group, and solid circles the Kurozu moromimatsu–treated group. (C) Tumor volume in Lovo cell–transplanted mice. Tumor volume was measured 8 wk after Lovo cell inoculation. The open bar indicates the control group, the solid bar the Kurozu-treated group, and the horizontally lined bar the Kurozu moromimatsu–treated group. Values are means ± SD. *$P < 0.001$ versus other groups.

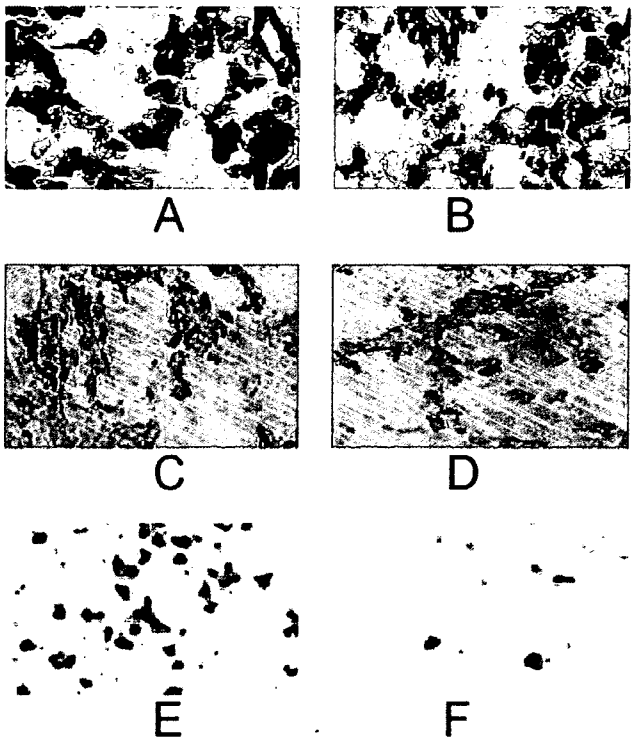

Fig. 2. Histologic examination of cancerous tissue after Lovo cell transplantation. Hematoxylin-eosin staining of tumor from (A) the control group and (B) the Kurozu moromimatsu–treated group. Terminal deoxynucleotidyl transferase-mediated dUTP nick end-labeling staining of tumor from (C) the control group and the (D) Kurozu moromimatsu–treated group. Nitrotyrosine staining of tumor from (E) the control group and (F) the Kurozu moromimatsu–treated group.

In the Lovo cell–transplanted model, the tumor volumes were 684.0 ± 34.0 mm^3 in the control group, 672.0 ± 56.0 mm^3 in the Kurozu group, and 273.0 ± 32.0 mm^3 in the Kurozu-M group ($P < 0.005$ for the Kurozu-M group versus control; Fig. 1C).

The following results refer to the Lovo cell–transplanted model.

HE staining, TUNEL staining, and nitrotyrosine immunostaining.

The HE staining showed no accumulation of polymorphonuclear leukocytes, which have been implicated in active oxygen production, in tumor tissue in the control group or the Kurozu-M group (Fig. 2A,B).

The TUNEL staining indicated that apoptosis in the Kurozu-M group was at the same level as that in the control group (Fig. 2C,D).

Because we previously found that nitrotyrosine, generated from peroxynitrite and tyrosine, is produced in human colon cancer [5], we examined whether the administration of Kurozu-M could inhibit nitrotyrosine formation. In the control group, many cells produced nitrotyrosine, whereas in the Kurozu-M group, only a few cells produced nitrotyrosine (Fig. 2E,F).

MMP-2 and MMP-9 assays

To investigate the role of MMPs in the action of Kurozu-M, we examined whether or not Kurozu-M altered the levels and activation of MMPs.

Total MMP-2 amounted to 8.8 ± 2.5 ng/mg of protein in the control group and 8.6 ± 2.8 ng/mg of protein in the Kurozu group. However, it was significantly reduced to 5.6 ± 1.8 ng/mg of protein by administration of Kurozu-M ($P < 0.05$ versus control; Fig. 3A). Activated MMP-2 amounted to 0.25 ± 0.06 ng/mg of protein in the control group, 0.27 ± 0.08 ng/mg of protein in the Kurozu group, and 0.12 ± 0.05 ng/mg of protein in the Kurozu-M group ($P < 0.05$ for the Kurozu-M group versus control; Fig. 3A).

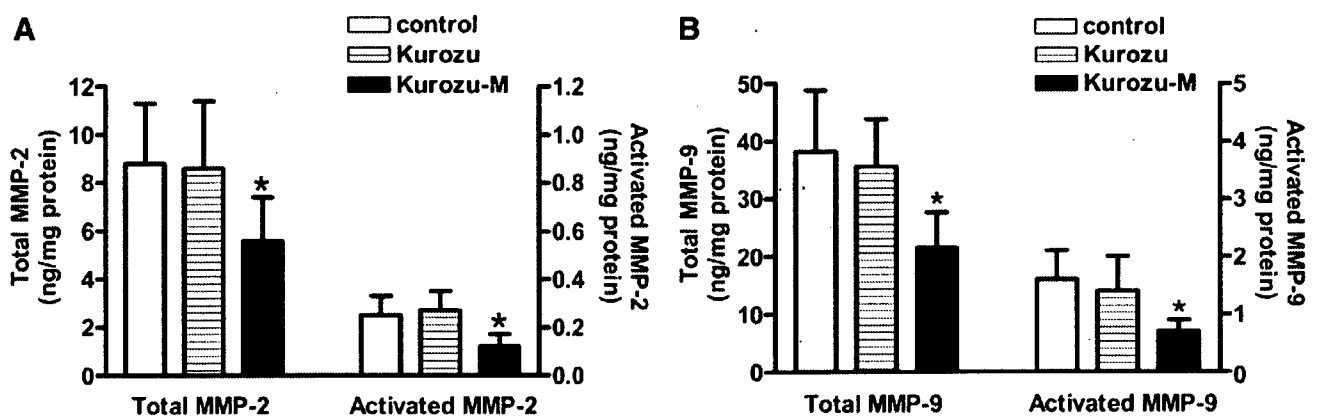

Fig. 3. Anti-metalloproteinase effect of Kurozu and Kurozu moromimatsu. (A) Total and activated metalloproteinase-2 in cancerous tissue after Lovo cell inoculation. The open bar represents the control group, the horizontally lined bar the Kurozu-treated group, and the solid bar the Kurozu moromimatsu-treated group. (B) Levels of total and activated metalloproteinase-9 in cancerous tissue after Lovo cell inoculation. The open bar represents the control group, the horizontally lined bar the Kurozu-treated group, and the solid bar the Kurozu moromimatsu–treated group. Values are means ± SD. $^*P < 0.001$ versus other groups.

Total MMP-9 amounted to 38.2 ± 10.6 ng/mg of protein in the control group and 35.6 ± 8.22 ng/mg of protein in the Kurozu group. However, it was significantly reduced to 21.5 ± 6.1 ng/mg of protein by administration of Kurozu-M ($P < 0.05$ versus control; Fig. 3B). Activated MMP-9 amounted to 1.6 ± 0.5 ng/mg of protein in the control group, 1.4 ± 0.6 ng/mg of protein in the Kurozu group, and 0.7 ± 0.2 ng/mg of protein in the Kurozu-M group ($P < 0.05$ for the Kurozu-M group versus control; Fig. 3B).

Discussion

Our results indicate that the administration of Kurozu-M inhibits the development of colon cancer in human colon cancer cell transplantation model in mice. Further, the administration of Kurozu-M inhibited nitrotyrosine production, decreased total MMP-2 and total MMP-9 levels, and inhibited activation of MMP-2 and MMP-9 in the lesion in this model.

Earlier studies had indicated that extract of Kurozu can inhibit chemical carcinogenesis [3,4,6]. However, in our study, the administration of Kurozu-M inhibited the development of colon cancer in a mouse model, whereas the administration of Kurozu did not prevent tumor growth. The major constituent of Kurozu is acetic acid, whereas the major component of Kurozu-M is a complex mixture of organic materials, including bacterial metabolites. The active components of Kurozu-M remain to be identified.

In this study, we found that administration of Kurozu-M inhibited production of nitrotyrosine in tumor tissue. Nitrotyrosine is generated through two pathways in vivo. One is the peroxynitrite pathway, in which tyrosine reacts with peroxynitrite to afford nitrotyrosine, and the second is the myeloperoxidase pathway, in which tyrosine reacts with myeloperoxidase and nitrite [7,8]. We previously reported that peroxynitrite is produced in human colon cancer tissue [5]. In contrast, myeloperoxidase is localized in polymorphonuclear leukocytes in vivo, but in this study we could not detect any accumulation of polymorphonuclear leukocytes by means of HE staining of cancerous tissue. Therefore, Kurozu-M administration may inhibit the peroxynitrite pathway. Possible mechanisms include inhibition of nitric oxide, superoxide, and/or peroxynitrite production, and scavenging of nitric oxide, superoxide, and/or peroxynitrite. Further work is needed to examine these possibilities.

The administration of Kurozu-M also inhibited MMP-2 and MMP-9 activity in cancerous tissue. These are representative gelatinases that contribute to the distant metastasis of cancer [9], and they are produced by cancer cells or macrophages [10]. A tetradecanoylphorbol acetate-responsive element is present in the promoter region of MMP-9 and is activated by various cytokines, such as interleukin and tumor necrosis factor [11]. In addition, MMP-9 is activated by nuclear factor-κB and MMP-2 [12]. MMP-2 is mainly activated by MT1-MMP, but recently it was shown that peroxynitrite also activates MMP-2 [13,14]. Kurozu-M may have inhibited cancer growth in our model through inhibition of peroxynitrite formation and MMP-2 and MMP-9 activities.

Kurozu moromimatsu was active against Lovo cells in this study, but not against DLD-1 cells. Lovo and DLD-1 cells differ not only in the degree of cellular differentiation but also in the expression of furin, which contributes to MMP activation [15]. The former line originates from well-differentiated adenocarcinoma and expresses furin protein, whereas the latter originates from poorly differentiated adenocarcinoma and does not express furin protein. It would be worth examining whether MMP activity is reduced in the absence of furin.

Conclusion

The administration of Kurozu-M inhibited tumor growth in a Lovo cell–transplanted mouse model and also inhibited nitrotyrosine production and activation of MMP-2 and MMP-9.

References

[1] Shimoji Y, Tamura Y, Nakamura Y, Nanda K, Nishidai S, Nishikawa Y, et al. Isolation and identification of DPPH radical scavenging compounds in Kurosu (Japanese unpolished rice vinegar). J Agric Food Chem 2002;50:6501–3.

[2] Shen X, Falzon M. PTH-related protein enhances LoVo colon cancer cell proliferation, adhesion, and integrin expression. Regul Pept 2005; 125:17–27.

[3] Shimoji Y, Kohno H, Nanda K, Nishikawa Y, Ohigashi H, Uenakai K, et al. Extract of Kurosu, a vinegar from unpolished rice, inhibits azoxymethane-induced colon carcinogenesis in male F344 rats. Nutr Cancer 2004;49:170–3.

[4] Nanda K, Miyoshi N, Nakamura Y, Shimoji Y, Tamura Y, Nishikawa Y, et al. Extract of vinegar "Kurosu" from unpolished rice inhibits the proliferation of human cancer cells. J Exp Clin Cancer Res 2004;23: 69–75.

[5] Szaleczky E, Pronai L, Nakazawa H, Tulassay Z. Evidence of in vivo peroxynitrite formation in patients with colorectal carcinoma, higher plasma nitrate/nitrite levels, and lower protection against oxygen free radicals. J Clin Gastroenterol 2000;30:47–51.

[6] Shimoji Y, Sugie S, Kohno H, Tanaka T, Nanda K, Tamura Y, et al. Extract of vinegar "Kurosu" from unpolished rice inhibits the development of colonic aberrant crypt foci induced by azoxymethane. J Exp Clin Cancer Res 2003;22:591–7.

[7] Eiserich JP, Hristova M, Cross CE, Jones AD, Freeman BA, Halliwell B, et al. Formation of nitric oxide-derived inflammatory oxidants by myeloperoxidase in neutrophils. Nature 1998;391:393–7.

[8] Fukuyama N, Takebayashi Y, Hida M, Ishida H, Ichimori K, Nakazawa H. Clinical evidence of peroxynitrite formation in chronic renal failure patients with septic shock. Free Radic Biol Med 1997; 22:771–4.

[9] Gullu IH, Kurdoglu M, Akalin I. The relation of gelatinase (MMP-2 and -9) expression with distant site metastasis and tumour aggressiveness in colorectal cancer. Br J Cancer 2000;82:249.

[10] Djonov V, Cresto N, Aebersold DM, Burri PH, Altermatt HJ, Hristic M, et al. Tumor cell specific expression of MMP-2 correlates

with tumor vascularisation in breast cancer. Int J Oncol 2002; 21:25–30.

[11] Steinbrenner H, Ramos MC, Stuhlmann D, Mitic D, Sies H, Brenneisen P. Tumor promoter TPA stimulates MMP-9 secretion from human keratinocytes by activation of superoxide-producing NADPH oxidase. Free Radic Res 2005;39:245–53.

[12] Wittrant Y, Theoleyre S, Couillaud S, Dunstan C, Heymann D, Redini F. Relevance of an in vitro osteoclastogenesis system to study receptor activator of NF-kB ligand and osteoprotegerin biological activities. Exp Cell Res 2004;293:292–301.

[13] Munoz-Najar UM, Neurath KM, Vumbaca F, Claffey KP. Hypoxia stimulates breast carcinoma cell invasion through MT1-MMP and MMP-2 activation. Oncogene 2005.

[14] Migita K, Maeda Y, Abiru S, Komori A, Yokoyama T, Takii Y, et al. Peroxynitrite-mediated matrix metalloproteinase-2 activation in human hepatic stellate cells. FEBS Lett 2005;579:3119–25.

[15] Deryugina EI, Ratnikov BI, Yu Q, Baciu PC, Rozanov DV, Strongin AY. Prointegrin maturation follows rapid trafficking and processing of MT1-MMP in Furin-negative colon carcinoma LoVo cells. Traffic 2004;5:627–41.